Phase feedback fringe projection profilometry for shiny objects

Rigoberto Juarez-Salazar[a,*], Fabio Vega[b,c], Sofia Esquivel-Hernandez[d], Victor H. Diaz-Ramirez[d], Andres G. Marrugo[b]

[a] *CONAHCYT—Instituto Politécnico Nacional, CITEDI, Av. Instituto Politécnico Nacional 1310, Nueva Tijuana, Tijuana, B.C. 22435, Mexico*
[b] *Facultad de Ingeniería, Universidad Tecnológica de Bolívar, Cartagena, 130001, Bolivar, Colombia*
[c] *Facultad de Electrónica, Universidad Popular del Cesar, Valledupar, 20005, Cesar, Colombia*
[d] *Instituto Politécnico Nacional, CITEDI, Av. Instituto Politécnico Nacional 1310, Nueva Tijuana, Tijuana, B.C. 22435, Mexico*

Abstract

Diffuse objects have suitable optical properties for accurate three-dimensional reconstruction by fringe projection profilometry. In contrast, shiny objects, such as glossy plastic items and metallic workpieces, are difficult to reconstruct due to image saturation. In this paper, the recursive structure of the hierarchical multi-frequency fringe projection profilometry is exploited to prevent saturation by a feedback loop. Novel functions for saturation, low-modulation, and grating intensity correction, suited to adjust the projector pixels inducing saturation, are proposed. The usefulness of the proposal is verified experimentally, confirming the high performance of the proposed phase feedback approach for the reconstruction of shiny objects.

Keywords:
Shiny objects, Saturation, Phase feedback, High dynamic range, Multi-frequency fringe projection.

---

1. Introduction

Fringe projection profilometry is a general term referring to a subset of structured light three-dimensional imaging techniques [1–3]. The main feature of fringe projection techniques is the use of two-dimensional cosine signals, known as fringe patterns, to obtain the object shape by phase demodulation [4]. These techniques can be categorized considering how the fringes are produced (e.g., interference [5], moire [6], defocusing [7], mechanically [8], and digitally [9]), the properties of light being exploited (e.g., wavelength/color [10] and polarization [11]), and the approach employed for fringe analysis (e.g., Fourier transform [12] and phase shifting [13], among others [14–16]).

The advent of digital projectors allowed full control of frequency and phase shifts of fringe patterns. Thus, digital projectors simplify the design and operation of fringe projection technology [17]. The high operation speeds of projectors and cameras allow for fast reconstruction of 3D objects, even when multiple phase-shifted fringe patterns are required. For simplicity, we refer to the digital fringe projection technique that employs phase-shifting wrapped phase extraction and multi-frequency phase unwrapping as fringe projection profilometry.

Nowadays, fringe projection profilometry is a prominent three-dimensional measuring tool that achieves high performance when diffuse objects are tested [18–20]. Since diffuse objects reflect incident light rays equally in all directions approximately [21], all object points are perceived with the same intensity regardless of the source and camera positions [22]. Therefore, images of diffuse objects reach the highest signal-to-noise ratio across all pixels [23]. In contrast, shiny objects reflect incident rays around their normal directions [24–26], leading to perceiving object points as bright or dark depending on the source and camera positions [27–29]. Since the signal-to-noise ratio in highlight and dark image regions is low [30–32], the performance of fringe projection systems is affected [33–35].

Modern applications of fringe projection profilometry require reconstructing shiny objects such as glossy plastic items and coins [36], metallic workpieces [37], aeroengine blades [38], porcelain crockery [39], and dental pieces [40]. These applications demand profilometers with an increased dynamic range [41–43]. Early high dynamic range fringe projection profilome-

---

[*] Corresponding author. Tel.: +52 664 623 1344
Email address: `rjuarezsa@conahcyt.mx` (Rigoberto Juarez-Salazar)

ters were produced by applying photometric techniques such as camera exposure [44] and projector brightness adjustment [45]. Later, profilometers were complemented with additional hardware, including polarizers [46], light modulators [47], and micromirror device cameras [48]. The hardware-based approach achieves good performance [49–51], but the optical setup becomes expensive and requires more effort to align, calibrate, and operate.

Alternatively, the algorithm-based approach avoids experimental complexity and excessive costs [52–54]. This approach comprises algorithms designed to process saturated images robustly [55, 56] or prevent saturation adaptively [57, 58]. High dynamic range profilometry by saturated image processing is simple to implement and recommended when the saturation is partial [59–61]. However, its usefulness is limited due to the mathematical restrictions of models for degraded image restoration [62]. On the other hand, instead of processing saturated images, advanced algorithms are employed to avoid saturation by adapting the grating intensity [63, 64]. These algorithms convert the profilometer into an adaptive system that optimizes itself for the specific object under test, reaching the highest dynamic range.

In broad terms, adaptive high dynamic range profilometers reconstruct an object in two steps [65–67]. First, a preliminary measurement is carried out to detect saturation and establish the image-slide map [68]. Then, the gratings are adapted to perform a second measurement using the optimized configuration [69]. Conventional methods use a binary saturation function extracted from the fringe pattern background light [70, 71] and apply a linear image-slide mapping using homographies [72, 73]. Binary background light saturation is unsuitable for fine adjustments of partially saturated pixels and loses precision due to the excluded saturation effects induced in the fringe amplitude. Also, the linear image-slide mapping would be inaccurate when complex shape objects are measured because the flatness assumption required by homographies is invalid [74]. Furthermore, the need for two reconstructions (preliminary and optimized) reduces the overall profilometer performance.

Fringe projection profilometry is currently supported by a wide range of fringe pattern processing methods [75]. Among them, hierarchical multi-frequency phase-shifting has emerged as a successful method for high-precision fringe projection profilometry [76–78]. This method works recursively, starting with coarse phase maps and ending with a high-quality phase map [17]. Although intermediate-phase maps have moderate accuracy, they provide sufficient information for suitable image-slide mapping, which helps to remove the need for a preliminary reconstruction.

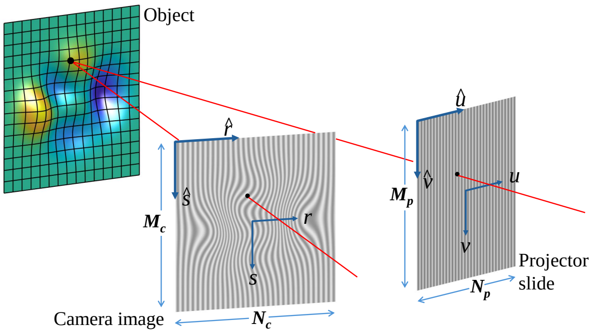

Figure 1: Simplified scheme of a typical fringe projection profilometer with an M_cN_c pixels camera and an M_pN_p pixels projector. Points on the image and slide planes are usually denoted by their pixel coordinates $(\hat{r}, \hat{s})$ and $(\hat{u}, \hat{v})$, respectively. Alternatively, the normalized coordinates (r, s) and (u, v) are used in this paper for convenience.

In this paper, a novel algorithm-based high dynamic range fringe projection profilometer is presented. The recursive structure of the hierarchical multi-frequency phase shifting method is exploited for saturation attenuation by a feedback loop. New continuous functions to detect saturation, low-modulation, and grating intensity correction are derived regarding the background light as well as the fringe amplitude. The theoretical principles are described, and the usefulness of the proposed method is verified experimentally. The experimental results confirm the outstanding performance of the proposed phase feedback loop in attenuating saturation and reconstructing bright areas of shiny objects.

The main contributions of this paper can be summarized as follows. First, a feedback loop for automatic pixel-wise projector intensity adjustment is developed. Second, new functions to detect saturation and low-modulation regions, considering both the background light and fringe amplitude, are proposed. Third, the background light underestimation phenomenon is discussed and addressed by weighting the fringe pattern intensities according to their closeness to the saturation level. Fourth, the grating intensity is corrected pixel-wise by a simple function and an interpolation-based image-slide mapping procedure.

2. Conventional fringe projection approach

This section explains the elementary blocks constituting a conventional fringe projection system: granting generator, wrapped phase extractor, phase unwrapping, phase normalization, and triangulation. Subsequently, the proposed phase feedback approach is presented in Section 3.

2.1. Grating generator

Consider a fringe projection profilometer consisting of a camera-projector pair, as depicted in Fig. 1. If the projector resolution is M_pN_p pixels, the slide points have pixel coordinates

$$(\hat{u}, \hat{v}) \in [1, 2, \cdots, N_p] \times [1, 2, \cdots, M_p], \tag{1}$$

where × denotes the Cartesian product. For convenience, the slide coordinates are normalized in the half-open interval

$$(u, v) \in (-1, 1] \times (-1, 1], \tag{2}$$

by transforming the projector pixel coordinates as

$$u = \frac{2}{N_p}\hat{u} - 1, \tag{3}$$

$$v = \frac{2}{M_p}\hat{v} - 1. \tag{4}$$

Considering the hierarchical multi-frequency phase-shifting method, the gratings $G_{i,j}$ and $H_{i,j}$ of "vertical" and "horizontal" fringes, respectively, with the i-th phase shift and the j-th frequency, are given as

$$\begin{aligned} G_{i,j}(u, v) &= \frac{1}{2} + \frac{1}{2}\cos\left[\omega_j u + \delta_i\right], \\ H_{i,j}(u, v) &= \frac{1}{2} + \frac{1}{2}\cos\left[w_j v + \delta_i\right], \end{aligned} \tag{5}$$

for

$$i = 1, 2, \cdots, m, \quad \text{and} \quad j = 1, 2, \cdots, n, \tag{6}$$

where m is the number of phase shifts, n is the number of frequencies, ω_j and w_j are the spatial frequencies, and δ_i is the i-th phase shift given as

$$\delta_i = \frac{2\pi}{m}(i - 1). \tag{7}$$

The spatial frequencies are calculated such that the first grating has a single fringe ($\omega_1 = w_1 = \pi$), the fringes in the last grating have a given period of λ pixels, and the frequency ratio between adjacent gratings is a constant ($\omega_{j+1}/\omega_j = \alpha$ and $w_{j+1}/w_j = \beta$). These constraints are met by the spatial frequencies

$$\omega_j = \pi\alpha^{j-1}, \tag{8}$$

$$w_j = \pi\beta^{j-1}, \tag{9}$$

where the constants α and β are defined as

$$\alpha = \left(\frac{N_p}{\lambda}\right)^{1/(n-1)}, \tag{10}$$

$$\beta = \left(\frac{M_p}{\lambda}\right)^{1/(n-1)}, \tag{11}$$

and λ is the number of pixels per fringe at the highest frequency. Block (**G**) in Fig. 2 represents the described grating generation stage.

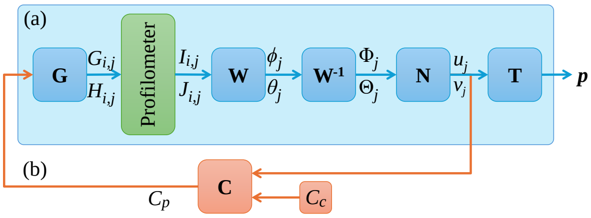

Figure 2: (a) Layout of the hierarchical multi-frequency phase-shifting fringe projection approach consisting of the blocks (G) grating generator, (W) wrapped phase extractor, (W^{-1}) phase unwrapper, (N) phase normalizer, and (T) triangulator. (b) Proposed phase feedback loop.

2.2. Background light and fringe amplitude estimation

The fringe patterns captured by the camera for each projected grating $G_{i,j}$ and $H_{i,j}$ are modeled, respectively, as

$$\begin{aligned} I_{i,j}(r, s) &= a_j(r, s) + b_j(r, s)\cos\left[\Phi_j(r, s) + \delta_i\right], \\ J_{i,j}(r, s) &= a_j(r, s) + b_j(r, s)\cos\left[\Theta_j(r, s) + \delta_i\right], \end{aligned} \tag{12}$$

where a_j and b_j are the background light and fringe amplitude, respectively, and the phases Φ_j and Θ_j carry information about the variables u and v, respectively. Following the method proposed by Bruning *et al* [79, 80], the functions a_j and b_j can be estimated from the captured fringe patterns as

$$a_j(r, s) = \frac{1}{2m}\sum_{i=1}^{m}\left[I_{i,j}(r, s) + J_{i,j}(r, s)\right], \tag{13}$$

$$\begin{aligned} b_j(r, s) = {} & \frac{1}{m}\left[\sigma^2(r, s; I_{i,j}) + \kappa^2(r, s; I_{i,j})\right]^{1/2} \\ & + \frac{1}{m}\left[\sigma^2(r, s; J_{i,j}) + \kappa^2(r, s; J_{i,j})\right]^{1/2}, \end{aligned} \tag{14}$$

where σ and κ are sine- and cosine-weighted sums of phase-shifted fringe patterns defined as

$$\sigma(r, s; F_{i,j}) = \sum_{i=1}^{m} F_{i,j}(r, s) \sin \delta_i, \tag{15}$$

$$\kappa(r, s; F_{i,j}) = \sum_{i=1}^{m} F_{i,j}(r, s) \cos \delta_i, \tag{16}$$

where $F_{i,j}$ is interchanged by the fringe patterns $I_{i,j}$ or $J_{i,j}$ in Eq. (14). The described background and amplitude estimations are contained by block (**W**) in Fig. 2.

2.3. Wrapped phase extraction and phase unwrapping

The phases Φ_j and Θ_j can only be obtained within the principal values $\phi_j, \theta_j \in (-\pi, \pi]$, known as *wrapped phase*, given as

$$\begin{aligned} \phi_j(r, s) &= -\tan^{-1}\left(\frac{\sigma(r, s; I_{i,j})}{\kappa(r, s; I_{i,j})}\right), \\ \theta_j(r, s) &= -\tan^{-1}\left(\frac{\sigma(r, s; J_{i,j})}{\kappa(r, s; J_{i,j})}\right), \end{aligned} \tag{17}$$

where $\tan^{-1}$ represents the four-quadrant inverse tangent applied to the input point-wise quotient. The wrapped phases $\phi_j(r, s)$ and $\theta_j(r, s)$ are outputs of block (**W**) in Fig. 2.

The hierarchical multi-frequency phase unwrapping method allows recovering the phase Φ_j and Θ_j from ϕ_j and θ_j using the previous unwrapped phase Φ_{j-1} and Θ_{j-1} as

$$\begin{aligned} \Phi_j(r, s) &= \phi_j(r, s) + 2\pi \left\lfloor \frac{\alpha\Phi_{j-1}(r, s) - \phi_j(r, s)}{2\pi} \right\rceil, \\ \Theta_j(r, s) &= \theta_j(r, s) + 2\pi \left\lfloor \frac{\beta\Theta_{j-1}(r, s) - \theta_j(r, s)}{2\pi} \right\rceil, \end{aligned} \tag{18}$$

where $\lfloor\cdot\rceil$ is the round operator. Since the gratings are designed so that the frequency at $j = 1$ is the unity, then the phases ϕ_1 and θ_1 are actually unwrapped; i.e.,

$$\begin{aligned} \Phi_1(r, s) &= \phi_1(r, s), \\ \Theta_1(r, s) &= \theta_1(r, s). \end{aligned} \tag{19}$$

Therefore, the initial condition of the recursive equations in (18) is

$$\begin{aligned} \Phi_0(r, s) &= 0, \\ \Theta_0(r, s) &= 0. \end{aligned} \tag{20}$$

The block labeled as ($\mathbf{W}^{-1}$) in Fig. 2 represents the described multi-frequency phase unwrapping process.

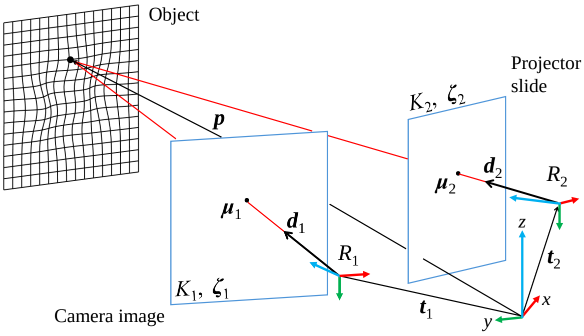

Figure 3: Point $\boldsymbol{p}$ determined by triangulation using the known correspondence $\boldsymbol{\mu}_1 \leftrightarrow \boldsymbol{\mu}_2$. The camera is characterized by the intrinsic matrix K_1, distortion parameters ζ_1, rotation matrix R_1, and translation vector $\boldsymbol{t}_1$. Similarly, the projector is characterized by the parameters K_2, ζ_2, R_2, and $\boldsymbol{t}_2$.

2.4. Phase normalization

The demodulated phases Φ_j and Θ_j are proportional to u and v, respectively, as can be seen from Eqs. (5) and (12). Therefore, the projector pixel coordinates are available by the simple normalization:

$$\begin{aligned} u_j(r, s) &= \frac{1}{\omega_j}\Phi_j(r, s), \\ v_j(r, s) &= \frac{1}{w_j}\Theta_j(r, s). \end{aligned} \tag{21}$$

Block (**N**) in Fig. 2 represents the described phase normalization process.

2.5. Point triangulation

The normalized phase establishes point correspondences between the image and slide planes. Namely, for any camera image point $\boldsymbol{\mu}_1 = (r, s)$, its associated projector slide point $\boldsymbol{\mu}_2 = (u, v)$ is obtained by Eq. (21). Hence, a point $\boldsymbol{p}$ on the object under test, associated with the given correspondence

$$\boldsymbol{\mu}_1 \leftrightarrow \boldsymbol{\mu}_2, \tag{22}$$

can be computed by triangulation, as shown in Fig. 3. Let K_1, ζ_1, R_1, and $\boldsymbol{t}_1$ be the intrinsic matrix, distortion parameters, orientation, and position of the camera, respectively. Similarly, let K_2, ζ_2, R_2, and $\boldsymbol{t}_2$ be the projector parameters. Since the camera and projector parameters can be obtained by a previous calibration [81–83], the direction vectors $\boldsymbol{d}_1$ and $\boldsymbol{d}_2$ can be obtained by

$$\begin{aligned} \boldsymbol{d}_1 &= \mathcal{D}(\boldsymbol{\mu}_1; K_1, \zeta_1, R_1), \\ \boldsymbol{d}_2 &= \mathcal{D}(\boldsymbol{\mu}_2; K_2, \zeta_2, R_2), \end{aligned} \tag{23}$$

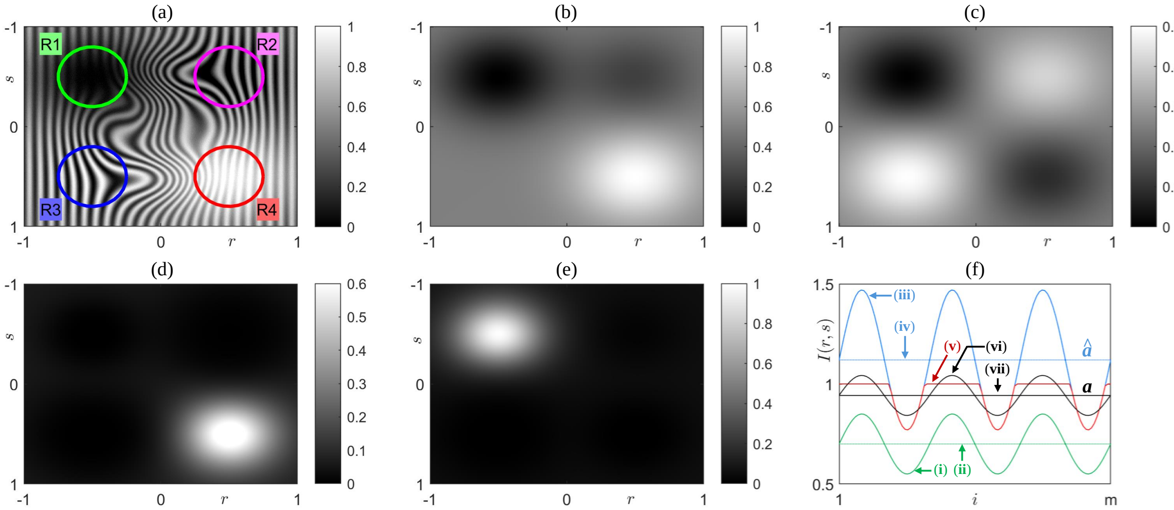

Figure 4: (a) Fringe pattern with typical degraded regions: (R1) black surface, unlit, or shadow, (R2) colored non-white surface, (R3) white Lambertian surface, and (R4) saturated fringes. (b) Background light. (c) Fringe amplitude. (d) Saturation function, Eq. (30). (e) Low-modulation function, Eq. (31). (f) Background light underestimation. (i) Unsaturated signal and (ii) its correctly estimated background. (iii) High-intensity signal and (iv) its actual background $\hat{a}$. (v) Available saturated signal, (vi) resultant fitted signal, and (vii) underestimated background a.

where $\mathcal{D}$ represents the distorted pinhole model defined as [84]

$$\mathcal{D}(\boldsymbol{\mu}; K, \zeta, R) = RK^{-1}\mathcal{H}[\boldsymbol{\mu}] + \left(\zeta_2\|\boldsymbol{\rho}\|^2 + \zeta_3\|\boldsymbol{\rho}\|^3 + \cdots\right)R\boldsymbol{e}_3, \tag{24}$$

with

$$\boldsymbol{\rho} = \mathcal{H}^{-1}[K^{-1}\mathcal{H}[\boldsymbol{\mu}]], \tag{25}$$

where $\mathcal{H}$ is the homogeneous operator [85], $\|\cdot\|$ denotes the Euclidean norm, $\boldsymbol{e}_3 = [0, 0, 1]^T$, $[\cdot]^T$ denotes transposition, and $[\cdot]^{-1}$ is the inverse. Fig. 3 shows that two solutions can be obtained for $\boldsymbol{p}$ as

$$\begin{aligned} \boldsymbol{p}_1 &= \boldsymbol{t}_1 + \ell_1\boldsymbol{d}_1, \\ \boldsymbol{p}_2 &= \boldsymbol{t}_2 + \ell_2\boldsymbol{d}_2, \end{aligned} \tag{26}$$

where the unknowns ℓ_1 and ℓ_2 can be estimated by solving the vector equation $\boldsymbol{t}_1 + \ell_1\boldsymbol{d}_1 = \boldsymbol{t}_2 + \ell_2\boldsymbol{d}_2$ using the least squares method as

$$\begin{bmatrix} \ell_1 \\ \ell_2 \end{bmatrix} = (D^T D)^{-1} D^T (\boldsymbol{t}_2 - \boldsymbol{t}_1), \tag{27}$$

with $D = [\boldsymbol{d}_1, -\boldsymbol{d}_2]$ being the regression matrix. Thus, the required vector $\boldsymbol{p}$ is defined as the average $(\boldsymbol{p}_1+\boldsymbol{p}_2)/2$ leading to [86]

$$\boldsymbol{p} = \frac{1}{2}DH\begin{bmatrix} \ell_1 \\ \ell_2 \end{bmatrix} + \frac{1}{2}(\boldsymbol{t}_1 + \boldsymbol{t}_2), \tag{28}$$

where $H = \mathrm{diag}(1, -1)$ is a 2-by-2 diagonal matrix. Block (**T**) in Fig. 2 represents the described point triangulation process.

The conventional hierarchical multi-frequency phase-shifting approach is depicted in Fig. 2(a). It is noteworthy that this approach reconstructs the object when all $2mn$ fringe patterns are available at $j = n$. However, small sets of $2m$ fringe patterns allow coarse reconstructions at $j = 1, \cdots, n-1$. Although the phase from reconstructions at $j < n$ has moderate accuracy, it is suitable for the image-slide mapping. This recursive structure is exploited by a phase feedback loop where, for each iteration j, the intensity correction function is computed to attenuate fringe saturation in the next iteration $j + 1$, as depicted in Fig. 2(b).

3. Phase feedback approach

3.1. Saturation and low-modulation functions

Fringe projection profilometry typically produces images with saturated regions and other degradations [87, 88], as illustrated in Fig. 4(a). Saturated regions can be identified using the background light and the fringe amplitude; see Figs. 4(b) and 4(c). Assuming that the image intensity is normalized within the closed interval $[0, 1]$, then the background light and twice the fringe amplitude are also normalized, i.e.,

$$\begin{aligned} a_j(r, s) &\in [0, 1], \\ 2b_j(r, s) &\in [0, 1]. \end{aligned} \tag{29}$$

Since saturation occurs when the background is high and the amplitude is low, see Figs. 4(a)-(c), we define the saturation function as

$$S_c(r,s) = a(r,s)[1-2b(r,s)], \tag{30}$$

where subscript c emphasizes that function S is on the camera image plane (r,s). Fig. 4(d) shows the proposed saturation function S_c. Analogously, since low-modulated pixels exhibit low values of both background and fringe amplitude, we define the low-modulation function as

$$L_c(r,s) = [1-a(r,s)][1-2b(r,s)], \tag{31}$$

which is high (close to unity) in low-modulated pixels and low (close to zero) otherwise. Fig. 4(e) shows the proposed low-modulation function L_c aimed at removing noisy pixels.

3.2. Background light underestimation

The background light is necessary to adjust the gratings on the projector and prevent saturation. Unfortunately, the background light is underestimated when saturated fringes are processed, as illustrated in Fig. 4(f). Let $\hat{a}$ be the actual background light of high-intensity fringes, and let a be the underestimated background obtained from the saturated fringes. A straightforward approach to determine the background light is by exploiting the linear response of the camera sensor [52]. Therefore, the actual background light in saturated regions is proportional to the underestimated one as

$$\hat{a}(r,s) = \tau a(r,s), \tag{32}$$

where τ is the underestimation parameter given by the user. Alternatively, the background light can be obtained by removing the saturated fringe patterns from the estimation process [70]. Moreover, we propose using all the fringe patterns but weighing their contributions according to their closeness to the saturation level. First, Eq. (13) is rewritten as the solution of a classical least squares problem as

$$a(r,s) = \frac{1}{2}\boldsymbol{e}_1^T (A^T A)^{-1} A^T [Y(r,s) + Z(r,s)], \tag{33}$$

where $\boldsymbol{e}_1^T = [1,0,0]$, the regression matrix is defined as

$$A = \begin{bmatrix} 1 & \cos\delta_1 & -\sin\delta_1 \\ 1 & \cos\delta_2 & -\sin\delta_2 \\ \vdots & \vdots & \vdots \\ 1 & \cos\delta_m & -\sin\delta_m \end{bmatrix}, \tag{34}$$

and, for every image point (r,s), the intensity data vectors Y and Z have a size of m-by-1, defined as

$$Y(r,s) = \begin{bmatrix} I_1(r,s) \\ I_2(r,s) \\ \vdots \\ I_m(r,s) \end{bmatrix}, \quad Z(r,s) = \begin{bmatrix} J_1(r,s) \\ J_2(r,s) \\ \vdots \\ J_m(r,s) \end{bmatrix}. \tag{35}$$

Note that the intensities vectors Y and Z in Eq. (33) contribute equally in the estimation of the background light $a(r,s)$. In contrast, we propose to apply the weighted least squares method as

$$\begin{aligned} \hat{a}(r,s) = {} & \frac{1}{2}\boldsymbol{e}_1^T \left[A^T Q_I(r,s) A\right]^{-1} A^T Q_I(r,s) Y(r,s) \\ & + \frac{1}{2}\boldsymbol{e}_1^T \left[A^T Q_J(r,s) A\right]^{-1} A^T Q_J(r,s) Z(r,s), \end{aligned} \tag{36}$$

where Q_I and Q_J are diagonal m-by-m weighting matrices defined as

$$Q_I(r,s) = \begin{bmatrix} 1-I_1(r,s) & & \\ & \ddots & \\ & & 1-I_m(r,s) \end{bmatrix}, \tag{37}$$

$$Q_J(r,s) = \begin{bmatrix} 1-J_1(r,s) & & \\ & \ddots & \\ & & 1-J_m(r,s) \end{bmatrix}. \tag{38}$$

Note that the intensities $I_i(r,s)$ and $J_i(r,s)$ are weighted by $1-I_i(r,s)$ and $1-J_i(r,s)$, respectively, which decreases as I_i and J_i approach the saturation level.

3.3. Grating intensity correction function

The maximum fringe contrast occurs when the background light and fringe amplitude are $1/2$. Since the actual background is $\hat{a}$, the correction factor for the grating G must be $1/(2\hat{a})$ at the saturated region, and 1, otherwise; i.e., $S_c G/(2\hat{a}) + (1-S_c)G$. Therefore, the grating intensity correction function can be defined as

$$C_c(r,s) = 1 - S_c(r,s) + \frac{S_c(r,s)}{2\hat{a}(r,s)} \tag{39}$$

Although the intensity correction function could be updated for each iteration j, it is advantageous to perform the estimation in an initializing stage using the grating with maximum frequency to reach the highest accuracy.

3.4. Image-slide mapping

It should be noted that the intensity correction function C_c is on the camera image plane (r,s). However, the correction function must be on to the projector slide

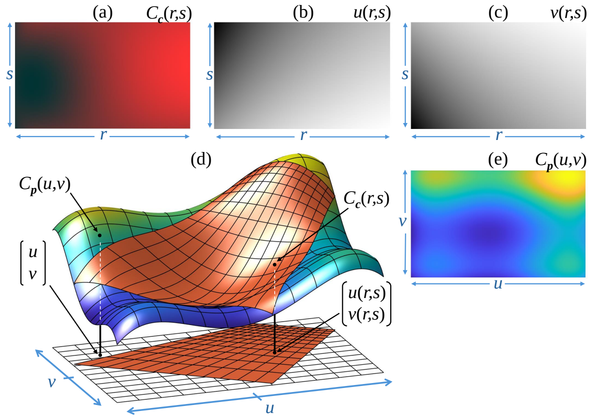

Figure 5: (a) Intensity correction function on the camera plane obtained by Eq. (39). (b) and (c) Projector pixel coordinates obtained from the demodulated phase by Eq. (21). (d) Interpolant C fitted by Eq. (40) for image-slide mapping. (e) Resultant intensity correction function on the projector plane obtained by Eq. (41).

plane (u, v) for grating intensity adjustment. The image-slide mapping is performed by interpolation using the coordinates $u_j(r, s)$ and $v_j(r, s)$ recovered by Eq. (21). Namely, let C_j be an interpolator fitted to the available data points $u_j(r, s)$, $v_j(r, s)$ and $C_c(r, s)$ as [89, 90]

$$C_c(r, s) = C_j[u_j(r, s), v_j(r, s)]. \tag{40}$$

Therefore, the intensity correction function on the slide plane is obtained by evaluating the interpolator at every projector pixel point as

$$C_{p,j}(u, v) = C_j(u, v). \tag{41}$$

Fig. 5 illustrates the described image-slide mapping process.

3.5. Grating intensity adjustment and summary

The correction function $C_{p,j}$ is employed to attenuate fringe saturation by pixel-wise intensity adjustment of the gratings $G_{i,j}$ and $H_{i,j}$ as

$$\begin{aligned} \tilde{G}_{i,j}(u, v) &= C_{p,j-1}(u, v)G_{i,j}(u, v), \\ \tilde{H}_{i,j}(u, v) &= C_{p,j-1}(u, v)H_{i,j}(u, v). \end{aligned} \tag{42}$$

The proposed phase feedback approach is summarized in the following seven steps. **Initialization**: (**S1**) Project $G_{i,j}$ with $j = n$ (highest frequency) and its m phase shifts to extract a and b, and generate the saturation function S_c by Eq. (30). It is worth emphasizing that neither $H_{i,j}$ nor lower frequency gratings need to be projected because phase demodulation is not required during the initialization stage. (**S2**) Apply Eq. (36) to

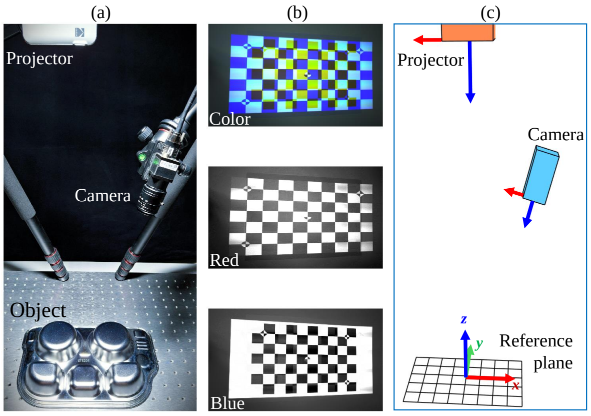

Figure 6: (a) Fringe projection profilometer reconstructing a shiny object. (b) One of thirty superposed color checkerboard images and its grayscale checkerboard images from the red and blue channels for projector and camera calibration, respectively. (c) Representation of the calibrated pofilometer using the estimated parameters.

estimate $\hat{a}(r, s)$ and compute $C_c(r, s)$ by Eq. (39). (**S3**) Set $j = 1$ and the initial values:

$$\begin{aligned} \Phi_0(r, s) &= 0, \\ \Theta_0(r, s) &= 0, \\ C_{p,0}(u, v) &= 1. \end{aligned} \tag{43}$$

Projection: (**S4**) Project $\tilde{G}_{i,j}$ and $\tilde{H}_{i,j}$ with their m phase shifts to extract ϕ_j and θ_j. (**S5**) Apply Eqs. (18) and (21) to obtain the projector slide coordinates u_j and v_j. (**S6**) Construct the interpolant C_j by Eq. (40), compute the function $C_{p,j}(r, s)$ by Eq. (41), and set $j = j + 1$. Repeat from step (S3) until $j = n$. **Reconstruction**: (**S7**) Compute an object point $\boldsymbol{p}$ for every point correspondence $(r, s) \leftrightarrow (u_n(r, s), v_n(r, s))$ using Eq. (28).

4. Experimental evaluation

The proposed phase feedback approach was evaluated experimentally by reconstructing a metallic object, as shown in Fig. 6(a). The profilometer was constructed using the camera iDS UI-3880CP-C-HQ (2076 × 3088 pixel resolution, 8 millimeter (mm) focal length imaging lens) and the projector Kodak Luma 150 (1080 × 1920 pixel resolution).

The profilometer was calibrated using the flexible camera-projector calibration method by superposed color checkerboards [91]. Two 7 × 10 checkerboards were employed: one on the reference plane (175 × 250 mm size and yellow color) and other on the slide plane (1080 × 1920 pixel size and blue color). Fig 6(b) shows one of the thirty-five captured checkerboard images and

Figure 7: Fringe patterns captured by (a) conventional fringe projection, (b) optimal camera exposure time, (c) the proposed phase feedback approach, and (d) the multi-exposure method. Four gratings ($j = 1, \cdots, 4$) with sixteen phase shifts each were projected. The initialization stage of the proposed method employed the highest frequency grating ($j = 4$) along the u-axis to obtain the correction function on the camera plane C_c while the correction function on the projector plane $C_{p,0}$ to the unity. In the projection stage, for each iteration j, the grating intensity was corrected using $C_{p,j-1}(u, v)$ from a previous iteration and getting $C_{p,j}(u, v)$ using C_c and the demodulated projector coordinates $u_j(r, s)$ and $v_j(r, s)$.

the gray-scale images extracted from its red and blue channels to calibrate the projector and camera, respectively. The system parameters were estimated by fitting the distorted pinhole model to the available checkerboard points [84]. The resultant calibration parameters were used to depict the calibrated system in Fig. 6(c). The following fringe projection experiments were performed using $m = 16$ phase shifts, $n = 4$ gratings, $\lambda = 12$ pixels per fringe at the grating highest frequency, and a linear piece-wise interpolants C_j.

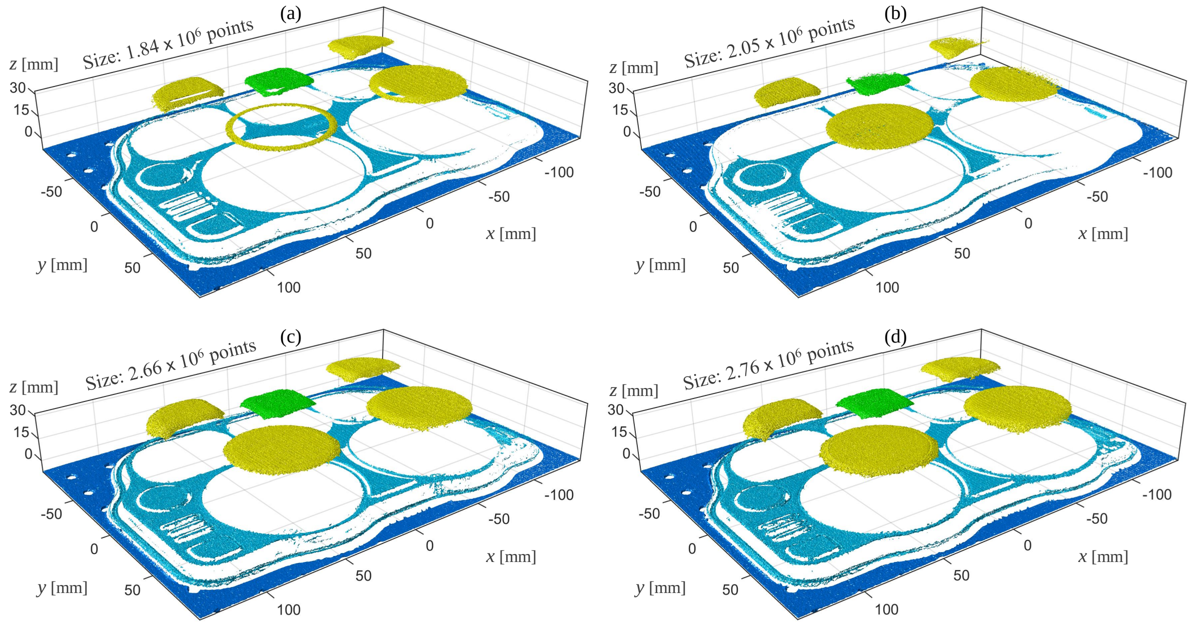

Figure 8: Three-dimensional reconstruction of a steel plate using (a) conventional fringe projection, (b) optimal camera exposure time, (c) the proposed phase feedback approach, and (d) the multi-exposure technique.

First, a shiny steel plate was reconstructed using the conventional fringe projection profilometry approach as a reference. Fig. 7(a) depicts the captured fringe patterns. It is worth noting that high intensity makes it possible to detect fringes in dark regions, but fringes are undetectable in saturated regions at $j = 4$. The saturation prevents phase extraction and impedes the recovery of the object surface in the saturated regions, as shown in Fig. 8(a). Similarly, the optimal exposure method was used to prevent saturation [52], as shown in Fig. 7(b). However, the fringes in low illumination regions are missed, degrading the three-dimensional reconstruction, as shown in Fig. 8(b).

Next, the reconstruction was performed using the proposed approach. **Initialization**. The grating $G_{i,4}(u, v)$, with $i = 1, \cdots, m$, was projected, obtaining the fringe patterns depicted in Fig. 7(c) (1st column). The extracted background light and fringe amplitude were employed to compute C_c. Also, the correction function on the projector plane C_p was initialized as the unity. **Projection**. The gratings $\tilde{G}_{i,j}$ and $\tilde{H}_{i,j}$ with $j = 1$ and all phase shifts were projected. The captured fringe patterns are depicted in Fig. 7(c) (2nd column). The demodulated projector pixel coordinates were used to obtain $C_{p,1}(u, v)$. This process was repeated for $j = 2, 3$, and 4, as depicted in Figs. 7(c) (3rd, 4th, and 5th columns). Note that both low illumination and fringe saturation issues were diminished effectively, as shown in Fig. 7(c) (6th column). **Reconstruction**. The projector pixel coordinates at the last iteration, $u_4(r, s)$ and $v_4(r, s)$, were used for triangulation. The resultant reconstruction is shown in Fig. 8(c), where a proper object reconstruction in the shiny regions is confirmed.

Additionally, the high dynamic range scanning technique by multiple camera exposure time was employed for comparison [44]. Fig. 7(d) shows the fringe patterns obtained after merging the images captured using ten exposure times, and Fig. 8(d) shows the resultant reconstruction. Note that this technique and the proposed method effectively detect fringes in low-illumination regions while preventing saturation, as shown in the last column of Figs. 7(c) and 7(d).

Further experiments were conducted to evaluate the performance of the proposed method in reconstructing objects of different materials. For this, a glossy plastic item and a ceramic mug with a textured surface were reconstructed, as shown in Figs. 9 and 10, respectively. Since the main issue in reconstructing shiny objects is the missed points from saturated and dark regions, the performance of the implemented methods was assessed considering the number of points constituting the three-dimensional reconstructions. The multi-exposure technique was used as the reference since it produced the largest point cloud size in all conducted experiments. Table 1 shows the quantitative results from the experi-

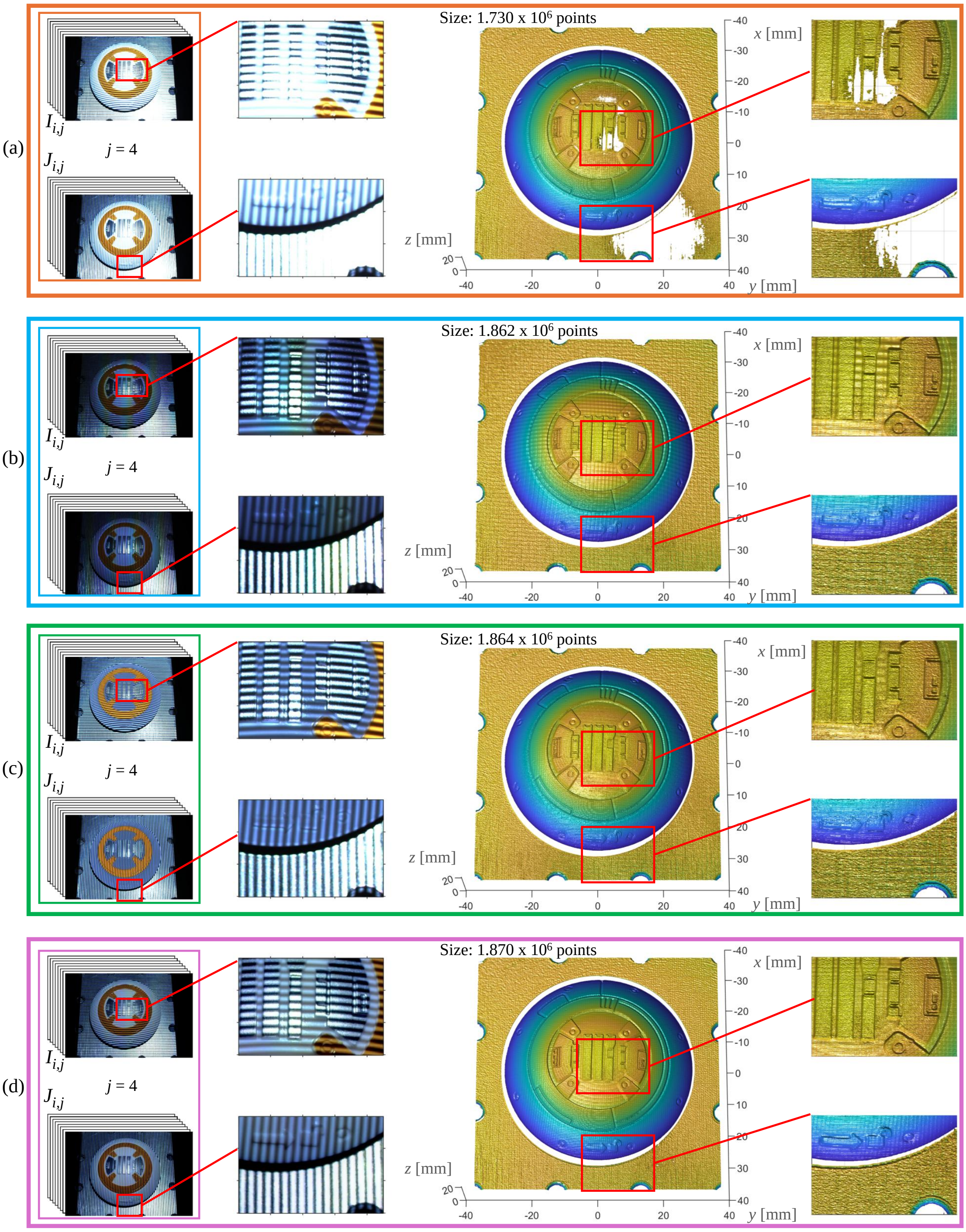

Figure 9: Highest fringe patterns and three-dimensional reconstruction of a glossy plastic item using (a) conventional fringe projection, (b) optimal camera exposure time, (c) the proposed method, and (d) the multi-exposure technique.

mental evaluation.

The experiments corroborate that reconstructing shiny objects is challenging using a single exposure time because fringes in saturation and low-illumination regions cannot be registered simultaneously. In contrast, the camera multi-exposure time method overcomes the

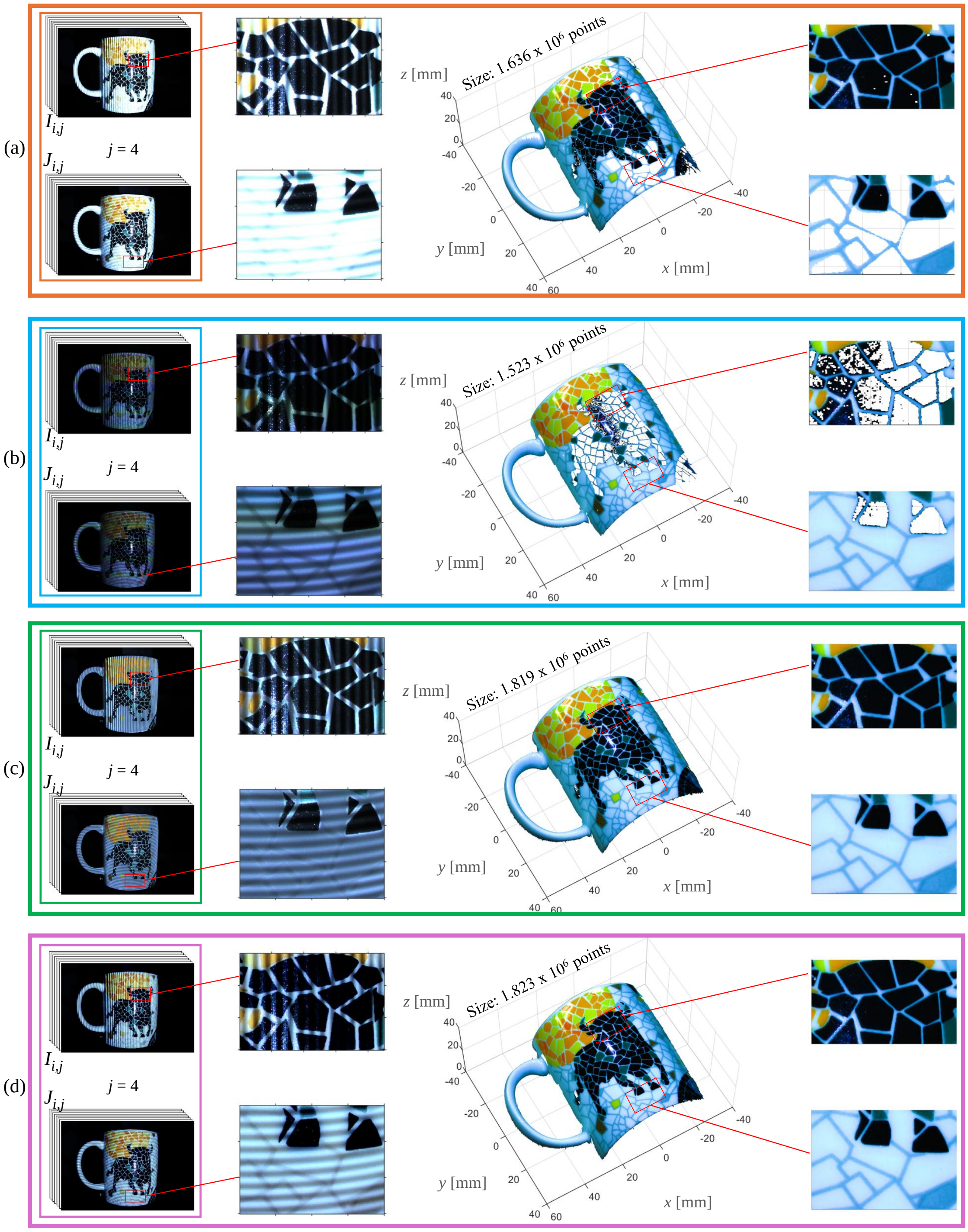

Figure 10: Highest fringe patterns and three-dimensional reconstruction of a textured ceramic mug using (a) conventional fringe projection, (b) optimal camera exposure time, (c) the proposed method, and (d) the multi-exposure technique.

high-dynamic issue at the cost of significantly increasing the number of required images. On the other hand, the proposed method is more effective in producing reliable reconstructions through pixel-wise projector intensity adjustments performed dynamically by a phase feedback loop during the projection stage.

	Steel	Plastic	Ceramic
Conventional	66.84 %	92.50 %	89.72 %
Optimal	74.34 %	99.55 %	83.56 %
Proposed	96.48 %	99.68 %	99.80 %

Table 1: Recovered points in the reconstruction of a steel plate, a plastic item, and a ceramic mug using conventional fringe projection, optimal camera exposure time, and the proposed method. The multiple camera exposure time technique was used as the reference.

5. Discussion

The main purpose of the initialization stage is to obtain the correction function C_c. This stage would be unnecessary if the background light and fringe amplitude extracted in the projection stage were used to compute C_c. However, since the saturation sensitivity increases with the grating frequency, the initialization stage allows projecting the highest frequency gratings to obtain C_c with high sensitivity and use it in the subsequent projection stage. Also, since the background light and fringe amplitude can be extracted by single-axis fringe projection, only the grating $G_{i,j}(u, v)$, with $j = n$, is used in the initialization stage.

Image-slide mapping has an intrinsic difficulty regarding the chosen interpolant function and the noise in the available data [92]. Although the linear piece-wise polynomial interpolation performed satisfactorily in this work, future research on an advanced method for outlier removal and image-slide mapping by approximation (instead of interpolation) should improve the precision of the proposed phase feedback approach.

6. Conclusion

A novel fringe projection profilometry approach suitable for reconstructing shiny objects was proposed. Three novel functions: saturation, low-modulation, and grating intensity correction, were derived regarding both the background light and fringe amplitude. A phase feedback loop was proposed to adjust the grating intensity and attenuate undesired saturation effects from shiny object reconstruction. The usefulness of the proposed approach was evaluated experimentally, confirming a successful object reconstruction in saturated regions. Desirable features of the proposed method, including simplicity and robustness, enabled it for modern engineering applications requiring optical reconstruction of shiny objects.

Declaration of Interest

The author declared that he has no known competing financial interests or personal relationships that could have appeared to influence the work reported in this paper.

Author contributions

R. Juarez-Salazar: Conceptualization, Methodology, Software, Data curation, Visualization, Writing - Original draft. **F. Vega:** Investigation. **S. Esquivel-Hernandez:** Formal analysis. **V.H. Diaz-Ramirez:** Funding acquisition, Writing - Review & Editing. **A.G. Marrugo:** Supervision, Writing - Review & Editing.

Funding

This work was supported by the *Consejo Nacional de Humanidades, Ciencias y Tecnologías* (CONAHCYT) (*Cátedras* CONACYT 880), and by Instituto Politécnico Nacional (SIP-20240319). F. Vega thanks Minciencias and Sistema General de Regalías (Programa de Becas de Excelencia) for a PhD scholarship.

Data availability

Data will be made available on request.

References

[1] C. Jiang, Y. Li, S. Feng, Y. Hu, W. Yin, J. Qian, C. Zuo, J. Liang, Fringe Projection Profilometry, Springer International Publishing, Cham, 2024, Ch. 14, pp. 241–286.

[2] A. G. Marrugo, F. Gao, S. Zhang, State-of-the-art active optical techniques for three-dimensional surface metrology: a review [Invited], J. Opt. Soc. Am. A 37 (9) (2020) B60–B77.

[3] J. Geng, Structured-light 3d surface imaging: a tutorial, Adv. Opt. Photon. 3 (2) (2011) 128–160.

[4] S. S. Gorthi, P. Rastogi, Fringe projection techniques: Whither we are?, Optics and Lasers in Engineering 48 (2) (2010) 133–140.

[5] E. B. Li, X. Peng, J. Xi, J. F. Chicharo, J. Q. Yao, D. W. Zhang, Multi-frequency and multiple phase-shift sinusoidal fringe projection for 3d profilometry, Opt. Express 13 (5) (2005) 1561–1569.

[6] K. Creath, J. Schmit, J. C. Wyant, Optical shop testing, 3rd Edition, John Wiley & Sons, Inc., 2007, Ch. Optical metrology of diffuse surfaces, pp. 756–807.

[7] S. Lei, S. Zhang, Flexible 3-d shape measurement using projector defocusing, Opt. Lett. 34 (20) (2009) 3080–3082.

[8] S. Heist, P. Lutzke, I. Schmidt, P. Dietrich, P. Kühmstedt, A. Tünnermann, G. Notni, High-speed three-dimensional shape measurement using gobo projection, Optics and Lasers in Engineering 87 (2016) 90–96.

[9] S. Zhang, Recent progresses on real-time 3D shape measurement using digital fringe projection techniques, Optics and Lasers in Engineering 48 (2) (2010) 149–158.

[10] Z. J. Geng, Rainbow three-dimensional camera: new concept of high-speed three-dimensional vision systems, Optical Engineering 35 (2) (1996) 376–383.

[11] G. Xiang, H. Zhu, H. Guo, Spatial phase-shifting profilometry by use of polarization for measuring 3d shapes of metal objects, Opt. Express 29 (13) (2021) 20981–20994.

[12] X. Su, W. Chen, Fourier transform profilometry: a review, Optics and Lasers in Engineering 35 (5) (2001) 263–284.

[13] C. Zuo, S. Feng, L. Huang, T. Tao, W. Yin, Q. Chen, Phase shifting algorithms for fringe projection profilometry: A review, Optics and Lasers in Engineering 109 (2018) 23–59.

[14] Q. Kemao, Windowed fourier transform for fringe pattern analysis, Appl. Opt. 43 (13) (2004) 2695–2702.

[15] M. Servin, J. A. Quiroga, M. Padilla, Fringe Pattern Analysis for Optical Metrology: Theory, Algorithms, and Applications, Wiley, 2014.

[16] E. Zendejas-Hernández, G. Trujillo-Schiaffino, M. Anguiano-Morales, D. P. Salas-Peimbert, L. F. Corral-Martínez, N. Tornero-Martínez, Spatial and temporal methods for fringe pattern analysis: a review, Journal of Optics 52 (2) (2023) 888–899.

[17] S. Zhang, High-Speed 3D Imaging with Digital Fringe Projection Techniques, CRC Press, Boca Raton, 2016.

[18] X. Zhao, T. Yu, D. Liang, Z. He, A review on 3d measurement of highly reflective objects using structured light projection, The International Journal of Advanced Manufacturing Technology 132 (9) (2024) 4205–4222.

[19] X. Liu, Z. Zhang, N. Gao, Z. Meng, 3d shape measurement of diffused/specular surface by combining fringe projection and direct phase measuring deflectometry, Opt. Express 28 (19) (2020) 27561–27574.

[20] D. Palousek, M. Omasta, D. Koutny, J. Bednar, T. Koutecky, F. Dokoupil, Effect of matte coating on 3d optical measurement accuracy, Optical Materials 40 (2015) 1–9.

[21] R. L. Cook, K. E. Torrance, A reflectance model for computer graphics, ACM Trans. Graph. 1 (1) (1982) 7–24.

[22] S. K. Nayar, X.-S. Fang, T. Boult, Separation of reflection components using color and polarization, International Journal of Computer Vision 21 (3) (1997) 163–186.

[23] T. Chen, H. P. A. Lensch, C. Fuchs, H.-P. Seidel, Polarization and phase-shifting for 3d scanning of translucent objects, in: IEEE Conference on Computer Vision and Pattern Recognition, 2007, pp. 1–8.

[24] R. M. Kowarschik, P. Kuehmstedt, J. Gerber, W. Schreiber, G. Notni, Adaptive optical 3-D-measurement with structured light, Optical Engineering 39 (1) (2000) 150 – 158.

[25] PingTan, Lin, L. Quan, H.-Y. Shum, Highlight removal by illumination-constrained inpainting, in: IEEE International Conference on Computer Vision, Vol. 1, 2003, pp. 164–169.

[26] Q. Hu, K. G. Harding, X. Du, D. Hamilton, Shiny parts measurement using color separation, in: K. G. Harding (Ed.), Two- and Three-Dimensional Methods for Inspection and Metrology III, Vol. 6000, 2005, p. 60000D.

[27] S. Feng, Q. Chen, C. Zuo, A. Asundi, Fast three-dimensional measurements for dynamic scenes with shiny surfaces, Optics Communications 382 (2017) 18–27.

[28] M. Li, Y. Cao, H. Wu, Three-dimensional reconstruction for highly reflective diffuse object based on online measurement, Optics Communications 533 (2023) 129276.

[29] G. Zhang, Y. Liu, Q. Yao, H. Deng, H. Zhao, Z. Zhang, S. Yang, Multi-view fringe projection profilometry for surfaces with intricate structures and high dynamic range, Opt. Express 32 (11) (2024) 19146–19162.

[30] Y. Chen, Y. He, E. Hu, Phase deviation analysis and phase retrieval for partial intensity saturation in phase-shifting projected fringe profilometry, Optics Communications 281 (11) (2008) 3087–3090.

[31] C. J. Waddington, J. D. Kofman, Modified sinusoidal fringe-pattern projection for variable illuminance in phase-shifting three-dimensional surface-shape metrology, Optical Engineering 53 (8) (2014) 084109.

[32] Z. Zhu, D. You, F. Zhou, S. Wang, Y. Xie, Rapid 3d reconstruction method based on the polarization-enhanced fringe pattern of an hdr object, Opt. Express 29 (2) (2021) 2162–2171.

[33] J. Xu, S. Zhang, Status, challenges, and future perspectives of fringe projection profilometry, Optics and Lasers in Engineering 135 (2020) 106193.

[34] Z. Zhu, P. Xiang, F. Zhang, Polarization-based method of highlight removal of high-reflectivity surface, Optik 221 (2020) 165345.

[35] Z. Zhu, M. Li, F. Zhou, D. You, Stable 3d measurement method for high dynamic range surfaces based on fringe projection profilometry, Optics and Lasers in Engineering 166 (2023) 107542.

[36] Z. Song, R. Chung, X.-T. Zhang, An accurate and robust strip-edge-based structured light means for shiny surface micromeasurement in 3-d, IEEE Transactions on Industrial Electronics 60 (3) (2013) 1023–1032.

[37] H. Zhao, X. Liang, X. Diao, H. Jiang, Rapid in-situ 3d measurement of shiny object based on fast and high dynamic range digital fringe projector, Optics and Lasers in Engineering 54 (2014) 170–174.

[38] H. Jiang, Q. Wang, H. Zhao, X. Li, High-precision composite 3d shape measurement of aeroengine blade based on parallel single-pixel imaging and high-dynamic range n-step fringe projection profilometry, Optics & Laser Technology 170 (2024) 110085.

[39] R. Benveniste, C. Unsalan, Single stripe projection based range scanning of shiny objects under ambient light, in: 24th International Symposium on Computer and Information Sciences, 2009, pp. 1–6.

[40] S. Chen, Intraoral 3-d measurement by means of group coding combined with consistent enhancement for fringe projection pattern, IEEE Transactions on Instrumentation and Measurement 71 (2022) 1–12.

[41] H. Lin, J. Gao, G. Zhang, X. Chen, Y. He, Y. Liu, Review and comparison of high-dynamic range three-dimensional shape measurement techniques, Journal of Sensors 2017 (1) (2017) 9576850.

[42] G. hua Liu, X.-Y. Liu, Q.-Y. Feng, 3d shape measurement of objects with high dynamic range of surface reflectivity, Appl. Opt. 50 (23) (2011) 4557–4565.

[43] H. Zhu, H. Guo, Surface profile measurement of metal objects by use of a fringe projection system with polarized dual projectors, Appl. Opt. 63 (30) (2024) 7883–7892.

[44] S. Zhang, S.-T. Yau, High dynamic range scanning technique, Optical Engineering 48 (3) (2009) 033604.

[45] H. Jiang, H. Zhao, X. Li, High dynamic range fringe acquisition: A novel 3-d scanning technique for high-reflective surfaces, Optics and Lasers in Engineering 50 (10) (2012) 1484–1493.

[46] S. Feng, Y. Zhang, Q. Chen, C. Zuo, R. Li, G. Shen, General solution for high dynamic range three-dimensional shape measurement using the fringe projection technique, Optics and Lasers in Engineering 59 (2014) 56–71.

[47] J. Jeong, M. Y. Kim, Adaptive imaging system with spatial light modulator for robust shape measurement of partially specular objects, Opt. Express 18 (26) (2010) 27787–27801.

[48] S. Ri, M. Fujigaki, Y. Morimoto, Intensity range extension

method for three-dimensional shape measurement in phase-measuring profilometry using a digital micromirror device camera, Appl. Opt. 47 (29) (2008) 5400–5407.

[49] B. Salahieh, Z. Chen, J. J. Rodriguez, R. Liang, Multi-polarization fringe projection imaging for high dynamic range objects, Opt. Express 22 (8) (2014) 10064–10071.

[50] X. Huang, J. Bai, K. Wang, Q. Liu, Y. Luo, K. Yang, X. Zhang, Target enhanced 3d reconstruction based on polarization-coded structured light, Opt. Express 25 (2) (2017) 1173–1184.

[51] Z. Zhu, Y. Dong, D. You, X. Sun, Accurate three-dimensional measurement based on polarization-defocused encoded structured light, Measurement 205 (2022) 112128.

[52] S. Zhang, Rapid and automatic optimal exposure control for digital fringe projection technique, Optics and Lasers in Engineering 128 (2020) 106029.

[53] Z. Song, H. Jiang, H. Lin, S. Tang, A high dynamic range structured light means for the 3d measurement of specular surface, Optics and Lasers in Engineering 95 (2017) 8–16.

[54] S. Feng, L. Zhang, C. Zuo, T. Tao, Q. Chen, G. Gu, High dynamic range 3d measurements with fringe projection profilometry: a review, Measurement Science and Technology 29 (12) (2018) 122001.

[55] M. Wang, G. Du, C. Zhou, C. Zhang, S. Si, H. Li, Z. Lei, Y. Li, Enhanced high dynamic range 3d shape measurement based on generalized phase-shifting algorithm, Optics Communications 385 (2017) 43–53.

[56] C. Waddington, J. Kofman, Analysis of measurement sensitivity to illuminance and fringe-pattern gray levels for fringe-pattern projection adaptive to ambient lighting, Optics and Lasers in Engineering 48 (2) (2010) 251–256.

[57] D. Li, J. Kofman, Adaptive fringe-pattern projection for image saturation avoidance in 3d surface-shape measurement, Opt. Express 22 (8) (2014) 9887–9901.

[58] F. Vega, A. G. Marrugo, Intelligent exposure time determination with structured light for accurate 3d object reconstruction, in: IEEE Colombian Caribbean Conference, 2023, pp. 1–5.

[59] E. Hu, Y. He, Y. Chen, Study on a novel phase-recovering algorithm for partial intensity saturation in digital projection grating phase-shifting profilometry, Optik 121 (1) (2010) 23–28.

[60] B. Chen, S. Zhang, High-quality 3d shape measurement using saturated fringe patterns, Optics and Lasers in Engineering 87 (2016) 83–89.

[61] H. Li, H. Wei, J. Liu, G. Deng, S. Zhou, W. Wang, L. He, P. Tian, Fringe projection profilometry based on saturated fringe restoration in high dynamic range scenes, Sensors 23 (6) (2023) 3133.

[62] X. Song, S. Zhang, Y. Wu, An accurate measurement of high-reflective objects by using 3d structured light, Measurement 237 (2024) 115218.

[63] S. Xu, T. Feng, F. Xing, Three-dimensional measurement method for high dynamic range surfaces based on adaptive fringe projection, IEEE Transactions on Instrumentation and Measurement 72 (2023) 1–11.

[64] J. Wang, Y. Yang, A new method for high dynamic range 3d measurement combining adaptive fringe projection and original-inverse fringe projection, Optics and Lasers in Engineering 163 (2023) 107490.

[65] H. Sheng, J. Xu, S. Zhang, Dynamic projection theory for fringe projection profilometry, Appl. Opt. 56 (30) (2017) 8452–8460.

[66] C. Chen, N. Gao, X. Wang, Z. Zhang, Adaptive projection intensity adjustment for avoiding saturation in three-dimensional shape measurement, Optics Communications 410 (2018) 694–702.

[67] T. Liu, W. Li, M. Tai, Y. Zhong, Three-dimensional measurement for specular reflection object based on adaptive fringe projection and phase measuring profilometry, Results in Optics 12 (2023) 100498.

[68] C. Chen, N. Gao, X. Wang, Z. Zhang, Adaptive pixel-to-pixel projection intensity adjustment for measuring a shiny surface using orthogonal color fringe pattern projection, Measurement Science and Technology 29 (5) (2018) 055203.

[69] H. Lin, J. Gao, Q. Mei, Y. He, J. Liu, X. Wang, Adaptive digital fringe projection technique for high dynamic range three-dimensional shape measurement, Opt. Express 24 (7) (2016) 7703–7718.

[70] C. Jiang, T. Bell, S. Zhang, High dynamic range real-time 3d shape measurement, Opt. Express 24 (7) (2016) 7337–7346.

[71] Y. Liu, Y. Fu, X. Cai, K. Zhong, B. Guan, A novel high dynamic range 3d measurement method based on adaptive fringe projection technique, Optics and Lasers in Engineering 128 (2020) 106004.

[72] G. Babaie, M. Abolbashari, F. Farahi, Dynamics range enhancement in digital fringe projection technique, Precision Engineering 39 (2015) 243–251.

[73] H. Lin, J. Gao, Q. Mei, G. Zhang, Y. He, X. Chen, Three-dimensional shape measurement technique for shiny surfaces by adaptive pixel-wise projection intensity adjustment, Optics and Lasers in Engineering 91 (2017) 206–215.

[74] S. Li, F. Da, L. Rao, Adaptive fringe projection technique for high-dynamic range three-dimensional shape measurement using binary search, Optical Engineering 56 (9) (2017) 094111.

[75] H. Liu, N. Yan, B. Shao, S. Yuan, X. Zhang, Deep learning in fringe projection: A review, Neurocomputing 581 (2024) 127493.

[76] C. Zuo, L. Huang, M. Zhang, Q. Chen, A. Asundi, Temporal phase unwrapping algorithms for fringe projection profilometry: A comparative review, Optics and Lasers in Engineering 85 (2016) 84 – 103.

[77] M. Zhang, Q. Chen, T. Tao, S. Feng, Y. Hu, H. Li, C. Zuo, Robust and efficient multi-frequency temporal phase unwrapping: optimal fringe frequency and pattern sequence selection, Opt. Express 25 (17) (2017) 20381–20400.

[78] Y. Hu, Q. Chen, Y. Liang, S. Feng, T. Tao, C. Zuo, Microscopic 3d measurement of shiny surfaces based on a multi-frequency phase-shifting scheme, Optics and Lasers in Engineering 122 (2019) 1–7.

[79] J. H. Bruning, D. R. Herriott, J. E. Gallagher, D. P. Rosenfeld, A. D. White, D. J. Brangaccio, Digital wavefront measuring interferometer for testing optical surfaces and lenses, Appl. Opt. 13 (11) (1974) 2693–2703.

[80] R. Juarez-Salazar, C. Mendoza-Rodriguez, J. E. Hernandez-Beltran, C. Robledo-Sanchez, How do phase-shifting algorithms work?, European Journal of Physics 39 (6) (2018) 065302.

[81] R. Vargas, L. A. Romero, S. Zhang, A. G. Marrugo, Calibration method based on virtual phase-to-coordinate mapping with linear correction function for structured light system, Optics and Lasers in Engineering 183 (2024) 108496.

[82] R. Juarez-Salazar, S. Esquivel-Hernandez, V. H. Diaz-Ramirez, Are camera, projector, and camera–projector calibrations different?, Applied Optics 62 (22) (2023) 5999–6006.

[83] S. Feng, C. Zuo, L. Zhang, T. Tao, Y. Hu, W. Yin, J. Qian, Q. Chen, Calibration of fringe projection profilometry: A comparative review, Optics and Lasers in Engineering 143 (2021) 106622.

[84] R. Juarez-Salazar, J. Zheng, V. H. Diaz-Ramirez, Distorted pinhole camera modeling and calibration, Applied Optics 59 (36) (2020) 11310–11318.

[85] R. Juarez-Salazar, V. H. Diaz-Ramirez, Operator-based homogeneous coordinates: application in camera document scanning, Optical Engineering 56 (7) (2017) 070801.

[86] R. Juarez-Salazar, G. A. Rodriguez-Reveles, S. Esquivel-

Hernandez, V. H. Diaz-Ramirez, Three-dimensional spatial point computation in fringe projection profilometry, Optics and Lasers in Engineering 164 (2023) 107482.

[87] Y. Long, S. Wang, W. Wu, K. Liu, Accurate identification of saturated pixels for high dynamic range measurement, Optical Engineering 54 (4) (2015) 043106.

[88] K. Zhong, Z. Li, X. Zhou, Y. Li, Y. Shi, C. Wang, Enhanced phase measurement profilometry for industrial 3d inspection automation, The International Journal of Advanced Manufacturing Technology 76 (9) (2015) 1563–1574.

[89] I. Amidror, Scattered data interpolation methods for electronic imaging systems: a survey, Journal of Electronic Imaging 11 (2) (2002) 157 – 176.

[90] K. S. Surana, Numerical methods and methods of approximation in sciencie and engineering, CRC Press Taylor & Francis Group, Boca Raton, 2019.

[91] R. Juarez-Salazar, V. H. Diaz-Ramirez, Flexible camera-projector calibration using superposed color checkerboards, Optics and Lasers in Engineering 120 (2019) 59–65.

[92] P. Xu, J. Liu, J. Wang, High dynamic range 3d measurement technique based on adaptive fringe projection and curve fitting, Appl. Opt. 62 (13) (2023) 3265–3274.